PFC/JA-82-18

X-RAY DIAGNOSTICS OF TOKAMAK PLASMAS

E. Källne and J. Källne

Plasma Fusion Center
Massachusetts Institute of Technology
Cambridge, MA 02139

September 1982

This work was supported by the U.S. Department of Energy Contract No. DE-AC02-78ET51013. Reproduction, translation, publication, use and disposal, in whole or in part by or for the United States government is permitted.

X-Ray Diagnostics of Tokamak Plasmas

Elisabeth Källne and Jan Källne
Harvard-Smithsonian Astrophysical Observatory
Cambridge, MA 02138 USA

1. INTRODUCTION

In this review, we will venture into a new arena for work in atomic X-ray spectroscopy which we can dub tokamak X-ray spectroscopy diagnostics (TOXRASD). Not only is the experimental development exciting, but the measurements explore areas of atomic and plasma physics which have been inaccessible until just recently. This, however, does not mean that spectroscopy of highly ionized atoms is lacking tradition; on the contrary, the pioneering work in this area goes back to the 40's and the soft X-ray studies of spark generated plasmas /1/. Even though much of the present experimental effort is oriented towards obtaining a TOXRASD for fusion conditions, the new results touch upon some very basic atomic physics questions as well. Much effort has gone into the study of few electron systems, i.e., H-, He-, and Li-like ions with the purpose of utilizing the characteristic X-ray emission for diagnosing laboratory and astronomical plasmas or with the aim of developing the diagnostics, i.e., extending our understanding of the relationship between X-ray line emission and the plasma conditions under which the ions are formed and their ground states excited. However, the emission from highly charged heavy ions, such as neon-like molybdenum, has also attracted interest. Several reviews have appeared describing the experimental programs and we will merely refer the reader to these /2-5/. Here we shall focus the discussion around results of the latest vintage from the TOXRASD project at the Alcator C tokamak at MIT.

2. PLASMA SOURCE

The plasma source can be characterized by the radial and temporal dependencies of the main parameters such as temperature (T_e) and densities (N_e,N_z) of electrons and ions. The plasma source is

confined by a toroidal magnetic field. However, through plasma-wall interactions, impurity ions are introduced to the plasma, which consists mainly of hydrogen, deuterium or helium. The impurity ions are successively ionized and distributed in the plasma volume determined by e.g. equilibrium conditions (e.g. coronal) and transport phenomena. The spatial distributions of these impurity ions can be characterized by shells of the individual ionization stages separated or overlapping in the plasma. Radial profiles of the emission from different ionization stages (see Fig. 1) will be dependent on plasma parameters /6-8/. In Fig. 1 the profiles of Cl^{15+} and Cl^{14+} at T_e = 1.4 keV are shown as predicted from coronal equilibrium and from a transport code /8/. The radial profiles of T_e and N_e are also included.

Attempts to predict the distribution of ions in the plasma are made on the assumption that the ions are in coronal equilibrium, i.e. ionisation and recombination processes balance each other. With knowledge of the radial and temporal distributions of electron density and temperature, it is possible to predict the impurity ion distributions from rate equations. It is therefore crucial to know the atomic cross sections involved. The impurities are transported from the walls and a steady state distribution is achieved after a time comparable to the energy confinement time (20-30 msec). The ions are assumed to be excited and ionized from their ground states. Atomic processes of importance are electron impact excitation and ionization from the ground state followed by radiative transitions, dielectronic and radiative recombination. The relative importance of these processes for certain plasma conditions is a point of investigation for TOXRASD. Furthermore, the influence of other possible processes such as proton excitation, charge exchange and ion-ion collisions need to be further investigated.

3. EXPERIMENTAL TECHNIQUES

Probing the plasma conditions by means of the emitted photons in the X-ray region is performed with mainly four different techniques: X-ray imaging /9,10/, X-ray continuum measurements /11,12/, survey

X-ray spectroscopy /2,13/ and high resolution, broad band line spectroscopy /14-17/. A typical time evolution of a plasma shot in Alcator C is shown in Fig. 2; each division along the abcissa is 10 ms. The fast rise of electron density (N_e) and plasma current (I_p) is followed by a stable period in which the plasma parameters are probed. The characteristic X-ray emission discussed in this paper is observed during this stable time period. However, during this apparently quiet period, there are internal instabilities developing with minor disruptions in the core of the plasma which can be imaged with the filtered X-ray diode arrays (SBD). With this technique, major m=1 ($\cos(m\theta)$ symmetry in poloidal angle) magneto-hydrodynamical instabilities (so-called sawteeth) have been observed /18/. Furthermore, X-ray imaging can provide precursory information for major disruptions of the plasma (terminating the discharge) and can give microscopic information on the origin of these disruptions. Emission from a pure plasma is dominated by the bremsstrahlung-recombination continuum. It can be measured with solid state pulse height analyzing detectors and the electron temperature is thus determined. Departures from the pure hydrogen bremsstrahlung continuum emission occur because of line emission superimposed on the continuum and because of effects in the high energy tail of the electrons causing an electron distribution of non-Maxwellian shape /19/. These two X-ray diagnostic methods thus give information on the position, homogeneity and stability of the impurity content as well as presence of high energy run-away electrons, etc. To detect a wide wavelength range in the soft X-ray region during single plasma discharges, a fast scanning crystal spectrometer has been developed at PLT /13/. With this diagnostic the radial distribution and the temporal evolution of emission from highly ionized low Z elements, such as oxygen, and from lower ionization stages of medium Z elements, such as iron, have been studied /20/. The first comparisons with predicted distributions, including transport effects, have shown general good agreement. The fourth technique of X-ray diagnostics is high resolution spectroscopy, which is in use at several major tokamak machines /14-16/. Mainly two different geometries have been used, focussing

Rowland circle and cylindrical van Hamos geometry. A schematic of the latter approach is shown in Fig. 3 /15/. We shall discuss some recent results obtained from the latter instrument at the Alcator C tokamak at MIT and their implications for future work.

4. ALCATOR RESULTS

The TOXRASD experiment has been taking data for about a year and the efforts have been directed towards good wavelength resolution $\Delta\lambda/\Delta \sim 1/3000$, large bandwidth, high sensitivity and high count rate. The data presented here was taken with a 10 cm long single wire proportional counter which limited the bandwidth to about 5% and the count rate to about 20 kHz. Much augmented spectroscopical and diagnostical performance can be achieved by detector improvements, which we shall discuss later. Our measurements of S, Cl and Mo impurities in the Alcator C tokamak /21/ (where these elements occur at trace element concentrations of about 10^{-5} N_e) cover the wavelength region 4.3-5.3 A. This region can be covered in three detector settings from which a composite spectrum can be formed as show in Fig. 4. This spectrum shows characteristic X-ray emission from S^{13+}, S^{14+}, Cl^{14+}, and Cl^{15+} as indicated and a host of lines from molybdenum between 28+ and 32+; the plasma conditions of these discharges were such as to enhance the Mo concentration in the plasma. From the extensive data material of spectra from several thousand discharges, we shall select a few examples to illustrate some poignant features of the results.

4.1 LINE IDENTIFICATION OF FEW ELECTRON SYSTEMS

H-Like Spectrum. The 1s-2p transition gives rise to the resonance lines $2S_{1/2} - 2P_{1/2, 3/2}$ (W'_H and W''_H) and dielectronic satellite lines $1s2p\,^1P_1 - 2p^2\,^1D_2$. We observe these for S^{14+} (see Fig. 5) at positions consistent with the predicted wavelengths of 4726.1, 4731.4 and 4783.6 mA /22,23/. Other satellites with a spectator electron in a higher orbit, i.e., transitions of the type $1sn - 2pn$, $n \geq 3$ are also indicated as a small foothill on the low energy side of the $^2S_{1/2} - ^2P_{1/2}$ resonance line.

He-like Spectra. The He-like spectrum was measured for both S and Cl (see examples in Figs. 6-9). These spectra are dominated by the $1s^2$-1s2p resonance line (w) $^1S_0$-$^1P_1$, the spin forbidden $^1S_0$-$^3P_1$ and the intercombination line $^1S_0$-$^3P_2$, (y and x, will here both be referred to as intercombination lines). Transitions are referred to with letter symbols in the conventional way /23,24/ (see also Appendix). The 1s-2s transition gives rise to the forbidden line (z) $^1S_0$-$^3S_1$. Several satellite lines to the resonance line with an extra (third) spectator electron in the 2s (lines q and r) or the 2p orbits (lines k and a) are observed. Some other satellite lines including the strongest, j, contribute to the spectrum but are hidden by the main lines (Fig. 8). The principal lines (w, x, y and z) and the satellite lines (q, r, a and k) are seen for both S and Cl with wavelengths as predicted. Excellent agreement is found with the results of Vainshtein /23/. Positive identification of these latter lines is provided by the spectra in Figs. 6-9.

We also note that while the Li-like charge states give rise to significant satellite lines to the w line in our S and Cl spectra, the corresponding satellites of Be-like charge states have escaped detection so far. They would be spread over a region of some 20 mA on the long wavelength side of the z line /27/. One such satellite has been observed in the spectrum of Fe from the plasma of the Princeton PLT tokamak /14/ which demonstrates the trend that the relative satellite intensity varies as Z^4, i.e., a factor of five increase between S and Fe when compared at temperatures of maximum emission for each atom.

The 1s-3p transition in sulphur is expected to produce a line at about 4.30 A which is just outside our range of measurements, but satellite lines to this resonance line (β) fall at somewhat longer wavelengths /25/. For certain plasma conditions as in Fig. 6 (low toroidal field, 40kG, low plasma current, 300 kA, N_e = 1.5 x $10^{14}cm^{-3}$, and T_e = 0.75 keV), we observe a clear peak at 4.388$\pm$0.001 A of a width consistent with that of a single line. This peak can be identified with the strongest satellite line of the 1s-3p transition, probably the transition $1s^22s$-1s2s3p calculated to be at

4.3895 A. We observe other distinct satellite lines in this region and we find a remarkable similarity with the spectrum /25/ from the laser produced plasma at conditions of $N_e = 10^{19}$ cm^{-3} and $T_e = 350$ ev.

4.2 LINE IDENTIFICATION OF MANY ELECTRON SYSTEMS

In the wavelength range 4.3-5.3 A we observe strong emission from molybdenum (the limiter material) under certain plasma conditions (see Fig. 4). A point of practical consequence is that the Mo impurity concentration depends strongly on plasma conditions and becomes rapidly important for low N_e-values while the S or Cl emission does not vary very much. Therefore we can deliberately vary the relative intensities of spectral lines of Mo and S/Cl, which is crucial for the identification of the weakest S and Cl lines, for instance the J satellite (see Fig. 5). Based on measurements and calculated wavelengths, we have identified 2p-3d, 2s-3p and 2p-3s transitions in charge states between 28+ and 32+ /26/. The most interesting components of the Mo emission are the Ne-like spectrum of Mo^{32+}, which is dominated by $2p_{1/2,3/2}$-3d transitions, and the strongest transitions identifying each charge state. We note that besides dominant principal transitions in the Mo spectrum, some contributions from dielectronic recombination satellites have been identified as well; for instance, the line at 4.837 A of Mo^{31+} /26/.

4.3 LINE INTENSITIES

<u>T_e and N_e Dependences.</u> Satellite line intensities (relative to the resonance line) depend on the electron temperature. For dielectronic satellites, this dependence goes approximately as $I_s'/I_w = 1/T_e$ and for inner shell excitation the I_s''/I_w ratio follows the abundance ratio N_{Li}/N_{He}. The N_{Li}/N_{He} ratio has a temperature dependence which can be calculated assuming a certain equilibrium for the plasma (coronal equilibrium) and certain ionization and recombination rates /27,28/. If the temperature T_e is known from the I_s'/I_w ratio or elsewhere, one can from the measured I_s''/I_w ratio determine the actual N_{Li}/N_{He} ratio which is the calculated N_{Li}/N_{He}

ratio for coronal equilibrium at the (ionization) temperature T_z. The difference T_z-T_e expresses whether the plasma is in a state of ionization ($T_z < T_e$) or recombination ($T_z > T_e$), i.e., whether the considered ion of charge state Z is superheated or supercooled in the plasma environment of given electron temperature.

An example with particularly strong satellites in the He-like spectrum of Cl is shown in Fig. 6. From the intensity $I_k = 0.177 \pm 0.015$, we determine a temperature of $T_e = 760$ eV with a statistical error of ± 50 eV. This determination of temperature is based on the most accurate calculations by Safronova /29/, other calculations /30/ give slightly lower values, $T_e = 630$ eV. The thus obtained temperature is consistent with $T_e = 650 \pm 150$ eV measured from the X-ray continuum shape /31/. Furthermore, we note that a satellite ratio I_a/I_k of 0.27 ± 0.05 agrees with the calculated one of 0.23. Other dielectronic satellites (see Fig. 8) are too small to be measured except for the j line whose influence on the z line can be estimated from the measured I_k and the calculated ratio $I_j/I_k = 1.4$ /29/. In Fig. 8 we have presented the calculated intensities of the strongest dielectronic recombination satellites relative to the k line with normalization to the observed I_k. The dotted curves for q and r include the inner shell excitation contribution assuming $T_e=T_z=760$ eV. The experimental spectrum is the same as in Fig. 6 apart from three-point smoothing of the raw data points. The calculated contribution of dielectronic recombination to the q line I_q' is 0.010 and that of inner-shell excitation is $I_q' = 0.029$ /29/. The total calculated intensity of q is 0.039 which amounts to only 50% of the measured ratio of $I_q = 0.073 \pm 0.015$. The situation is similar for the r satellite where $I_r' + I_r'' = 0.02+0.012 = 0.032$ /29/ compared to a measured value of 0.053 ± 0.017. We have thus found that the calculated I'' values are too low indicating that the plasma is ionizing with a nominal T_z of about 420 eV with reservation, however, for possible difference in radial profiles between Cl^{14+} and Cl^{15+} ions. This is a general feature for most of our spectra at lower temperatures that $I_q(exp) > I_q(theor)$ at given T_e, indicating that this is a characteristic feature of the plasma we observe or perhaps one should check for theoretical problems with the predicted rates of

inner shell excitations.

Fig. 6 shows another example with significant satellite intensities but at a systematically lower relative level than for Fig. 7. From I_k/I_w, we determine $T_e = 940\pm80$ eV (compared to 1050 ± 150 eV from X-ray continuum measurements /31/) and the temperature difference is reflected in the overall satellite intensity difference. Another reason for comparing these particular spectra is, however, the change in density from 1.5 to 3.0×10^{14} cm^{-3} in going from Fig. 6 to 7, which is of interest with regard to the line intensity ratio R = z/x+y. We find this ratio to be 1.20 ± 0.14 and 0.97 ± 0.07 after corrections for the satellite interferences as discussed above and shown in Fig. 8. The calculated values are 1.37 and 0.92 where the difference comes from the collisional population transfer between the long lived triplet n=2 states, i.e. ^3S-^3P, which is density dependent; the collisional and radiative rates are comparable at densities $N_e = 3 \times 10^{14}$ cm^{-3} /32,33/.

With the above two examples, we have demonstrated that the He-like spectra of Cl (and the same is true for S) contain information on T_e and N_e. The statistical accuracy with which we can measure the relative intensities of k/w and z/x+y is a matter of data accumulation rate per single discharge, or over how many constant discharges one can accumulate data. In the latter case, the crucial question is that of reproducibility of plasma discharges which we shall address below. With regard to the theory, the atomic rates computed and models used appear to give a good overall description of the plasma dependence of the present (as well as of previous) observations, except for the satellites due to inner shell excitation.

Comparison of 1s-2p and 1s-3p Transitions. The He-like spectrum for sulphur of n=2 upper states appear in the λ range 5.03 to 5.11 A and is similar to that of Cl already discussed (see Fig. 9). The 1s-3p resonance line of the He-line S (β) is located at $\lambda \simeq 4.30$ A /25/, which is just outside the spectrometer bandwidth ending at 4.31 A. Since this line is of diagnostics interest we can estimate

its intensity relative to the observed satellite peak as well as to the 1s-2p resonance. We use the results in Fig. 7 obtained at T_e = 960 eV. From the observed satellite to resonance intensity of 0.91 in the laser plasma at T_e = 350 eV and the calculated T_e dependence /25/ we determine the relative satellite intensity to be 0.09 at T_e = 960 eV; i.e., the 1s-3p resonance line in Fig. 7 should be 11.4 times the satellite line. The 1s-2p resonance line for S was measured during other but similar discharges of the same run 0805. Assuming constant S emission, we determine the 1s-3p to 1s-2p intensity ratio to be 0.5 ± 0.2.

The Temperature of Electrons and Ions. For the run 0303 we have determined the electron temperature in four ways. The spectrum in Fig. 10 shows the resonance lines of H-like and He-like S; these lines are broader than normal because of larger detector contribution at the extreme ends. We determine the ratio of $I_W/I_w = 0.75\pm0.07$, which implies a temperature of $T_e = 2.1\pm0.2$ keV assuming that the N_H/N_{He} abundance ratio is in coronal equilibrium /35/. From the satellite ratio in the same figure, one determines as $I_J/I_W = 0.040\pm0.012$ and a temperature of 1.7 ± 0.3 keV. From another but similar discharge we recorded the He-like S spectrum shown in Fig. 9. From this single discharge spectrum we determine $I_k/I_w = 0.014\pm0.01$ and the statistical error can be improved to 0.012 ± 0.007 by adding three consecutive, similar discharges. The corresponding temperature is 2.3 ± 0.5 keV. Finally, the I_q/I_w ratio is found to be $0.016\pm.006$, which corresponds to a temperature of 1.8 ± 0.6 keV with a N_{13+}/N_{14+} abundance ratio of S given by coronal equilibrium. We thus find consistency between the four different spectroscopic determinations of electron temperature. The results can be used for testing the underlying atomic physics calculations and to judge the ion abundance ratio relative to that of coronal equilibrium, i.e., the ionization equilibrium or departure from the same. At high temperatures, the results on q suggest a plasma closer to ionization equilibrium between Li- and He-like sulphur than would be the case for lower T_e. The intensity ratios and the deduced temperatures are a first attempt to check consistency in these data and explore the possibilities of TOXRASD. For a complete analysis

the radial distributions of the different ionization stages need to be considered.

A parameter of crucial importance for plasma fusion is the ion temperature (T_i) or even more so is information on the relationship between T_i and T_e. A well separated single line in the X-ray spectrum can be used to determine Doppler broadening due to the thermal motion of the ions. The resonance line w is a good candidate for this purpose, especially for higher temperatures where the $n\geq 3$ foot hill satellites are small (see Figs. 9 and 11), and the y and z lines can provide complementary information. The line width in Fig. 9 (from run 0303) is determined to be 7.3 ± 0.3 channels which can be improved to 7.2 ± 0.15 (corresponding to 3.1 mA) using an average of three discharges. From this we determine $T_i=1.4\pm.1$ keV having subtracted the estimated instrumental resolution corresponding to 630 eV. With this result, we have demonstrated that one can achieve simultaneous spectroscopial measurement of T_e and T_i of sufficient statistical accuracy to see differences between the two temperatures. With reservation for not yet unravelled systematic errors, our results suggest that the thermal coupling between electrons and ions is not 100% effective even for ohmically heated plasmas at relatively high electron densities.

Ionization Equilibrium. The line ratio $g = I_q/I_w$ is a predictable function of T_e for an ion abundance ratio N_{14+}/N_{15+} (to choose the Cl case) in coronal equilibrium. Knowing the temperature, the difference between experiment and calculation tells us about the departure from coronal equilibrium (T_z-T_e). The ratio G = x+y+z/w is temperature dependent because of a difference in temperature dependence of the triplet and singlet impact excitation rates /32/. G has also been predicted to depend on T_z-T_e because of the larger recombination contribution to the triplet state, so G would reflect T_z-T_e too. We thus have two line ratios relating to T_z-T_e, which we consider for the low and high temperature, T_e = 0.7 and 2 keV, cases of the He-like chlorine spectrum shown in Figs. 6 and 11. At the low temperature, we find G $=0.94\pm.05$ compared to the predicted /32,33/ value of G = 0.96 with no recombination. As mentioned already, we

have determined $q_{exp} > q_{th}$ so both these results suggest a plasma under ionization or that the N_{14+}/N_{15+} ratio is larger than that of coronal equilibrium. At the high temperature, we determine $G=0.59\pm0.04$ compared to the predicted value of 0.45 which increases to 0.55 if recombination is included /33/. In this case, the experimental value of g (as stated above) is consistent with the prediction, so that both the g and G parameters indicate less departure from ionization equilibrium at the higher temperature. The parameters reflecting T_z-T_e and their experimental determination are probably closely related to ion diffusion effects, i.e., this information has a bearing on the important question of transport in the plasma and hence confinement times.

Intensity Variations of Mo Lines. On the basis of wavelength, we have preliminarily identified lines from molybdenum in charge states from 28+ to 32+ /26/. It is clear that the temperature dependent intensity variation of lines will show the characteristics of the particular charge state involved which can help in the line identification. Assuming that we know the temperature of the plasma in the region of the emission studied, the line ratios can aid in the identification. Assuming instead that the line identification is known, plasma diagnostics information can be deduced. Examples of data that can be used in this context are shown in Fig. 12. The J satellite line has an intensity relative to the W resonance which determines $T_e = 1.6\pm.4$ and 1.9 ± 0.2 keV for the cases 12a and 12b. The intensity ratio of dominant 2p–3d lines in Mo^{30+} to Mo^{32+} changes between 0.5 and 2. It is clear that the observed variation of the Mo^{30+}/Mo^{32+} intensity ratio is not consistent with the identification made. However, the temperature given by J refers to the plasma region of maximum emission from the S^{13+} ions (cf. Fig. 1) which can differ from the radial distribution for $Mo^{30+,32+}$ and the two Mo species can be spatially separated too. Therefore, the line identification for many electron systems such as Mo is a complicated business and the temperature dependence must be used judicially. Once the identification is clear and a systematic of temperature dependences emerge, we can hope to use these complicated line spectra for detailed radial plasma mapping.

Intensity Variations of Fine Structure Components. We have furthermore measured the intensity ratio of the fine structure components of the H-like resonance lines for S ($^2S_{1/2}$-$^2P_{1/2,3/2}$) and of the intercombination transition of He-like S and Cl ($^1S_0$ - $^3P_{1,2}$). The intensities are predicted to split according to statistical weights, i.e., without preference for angular momentum of the upper state of the transition; the predicted /32,33/ intensity ratios are $^2P_{1/2}/^2P_{3/2}$ = 0.5, and $w^3P_2/^3P_1$ = 0.52 and 0.65 for S and Cl. Our average values for many discharges are generally not far from these predictions but drastic variations are observed in shot-to-shot comparisons. Examples are shown in Figs. 13 and 14 The explanations for these variations are still at large. It is neither clear which atomic population processes could be at play here nor do we know enough about the plasma conditions affecting these ratios. For the $^3P_2/^3P_1$ ratio the typical variation range is from 0.3 to 1.3 (similar for both S and Cl). Theoretically we have only been able to come up with a 10% difference in this ratio assuming proton collisonal coupling between the n=2 triplet states /33/. Proton collisons have previously been predicted to couple the 2s and 2p states of H-like ions and hence increase the $^2P_{1/2}/^2P_{3/2}$ intensity ratio with increasing proton (i.e., also electron) density /27/. However, the proton effects appear too small to explain the observed variations let alone that the change is only in one direction. Here, we need to make simultaneous measurements of these two ratios to see if the variations are correlated and hence answer the question whether there is a common cause affecting these line ratios. These results are both experimentally clear and interpretationally puzzling and should entice some stretching of the atomic physics imagination.

5. NEXT GENERATION TOXRASD MEASUREMENTS

The results from the new TOXRASD experiment at the Alcator C tokamak and those from the well established experiment at the Princeton tokamak have already yielded valuable diagnostics information and touched upon interesting atomic physics questions. However, they also indicate the potential for further development to probe the plasma and the atomic processes in greater detail. For our

project the limit has been on the detector side which we now hopefully have solved with the development of a new fast delay line x-y detector /36/; similar, the Princeton Bragg spectrometer has been augmented with a new detector. Together with a fast CAMAC data acquisition we hope to achieve count rates of 0.2 to 1 MHz. The new detector is 25 cm long and can detect about 0.8 mA of our spectrum shown in Fig. 4 at an expected resolution of better than 0.2 mm or (<0.4 mA at 4.4 A). This will allow measurements of high resolution, broad band spectra with an expected statistical accuracy of better than 3% for dominant lines for single Alcator discharges. The objective here is to measure accurately the line width of several lines simultaneously (and hence the ion temperature) and its correlation with the electron temperature deduced from various line ratios. With the many line ratios one can then study simultaneously, the plasma presents a unique atomic physics laboratory where the excited states involved in the transitions observed are subjected to the same and (partially) controllable medium of hot electrons and ions which is sustained for a long period of time on the scale of atomic relaxation times. Once the detector system can handle high count rates it is natural to probe the time evolution of the line emission for single plasma discharges. Thanks to the high light collection efficiency of the van Hamos geometry of our spectrometer (and to H. Schnopper /37/ who originated this spectrometer idea for TOXRASD), we expect to achieve 5 to 10% statistical accuracy for strong lines for a time resolution of 10 ms, which can be augmented by increasing the crystal height and the viewing solid angle into the plasma, etc. With the extended band width and time information, one would be able to measure the time correlation between the intensity ratios x/y and $W_{1/2}/W_{3/2}$ and determine the cause of the variations we observe in these ratios for seemingly constant shots and hopefully reveal the atomic process affecting these states and the hidden parameter that varies for seemingly constant plasma shots. Results of the type presented (including measurements and atomic physics interpretations) and the realization of time resolved spectroscopy are important for plasmas heated by other measures than ohmic heating. The Princeton group has already measured He-like Fe spectra

for plasmas heated by neutral ion injection /38/. Under these conditions one surely disturbs the plasma equilibrium and simultaneous measurements of T_i, T_e, and T_z as a function of time provides a real challenge for time resolved TOXRASD measurements and should be of great atomic physics interest, too. The highly ionized atoms are effective sensores distributed over the whole plasma volume. The information is encoded in the form of characteristic line-spectra and we are making rapid progress in increasing the accuracy of the measurements and finding the formula for decoding the TOXRASD spectra.

ACKNOWLEDGEMENTS

We have greatly benefitted from the stimulating support by Ron Parker and the Alcator group. We also wish to thank M. Bitter for sharing recent data with us, R. Petrasso for results on X-ray imaging, and John Rice for providing the results on radial profiles. The work was supported by the U.S. Department of Energy.

Appendix I

Key to the main lines and satellites of the H- and He-like spectra. All satellites are due to dielectronic recombination apart for those marked with an asterick.

Spectrum	Letter Key	Multiplet transition
H-like	$W(P_{3/2})$	$2p\ ^2P_{3/2} - 1s\ ^2S_{1/2}$
	$W(P_{1/2})$	$2p\ ^2P_{1/2} - 1s\ ^2S_{1/2}$
	J	$2p^2\ ^1D_2 - 1s2p\ ^1P_1$
He-like	w	$1s2p\ ^1P_1 - 1s^2\ ^1S_0$
	x	$1s2p\ ^3P_2 - 1s^2\ ^1S_0$
	y	$1s2p\ ^3P_1 - 1s^2\ ^1S_0$
	z	$1s2s\ ^3S_1 - 1s^2\ ^1S_0$
	j	$1s2p^2\ ^2D_{5/2} - 1s^22p\ ^2P_{3/2}$
	k	$1s2p^2\ ^2D_{3/2} - 1s^22p\ ^2P_{1/2}$
	l	$1s2p^2\ ^2D_{3/2} - 1s^22p\ ^2P_{3/2}$
	a	$1s2p^2\ ^2P_{3/2} - 1s^22p\ ^2P_{3/2}$
	b	$1s2p^2\ ^2P_{3/2} - 1s^22p\ ^2P_{1/2}$
	c	$1s2p^2\ ^2P_{1/2} - 1s^22p\ ^2P_{3/2}$
	d	$1s2p^2\ ^2P_{1/2} - 1s^22p\ ^2P_{1/2}$
	q*	$1s(2s2p^1P)^2P_{3/2} - 1s^22s\ ^2S_{1/2}$
	r*	$1s(2s2p^1P)^2P_{1/2} - 1s^22s\ ^2S_{1/2}$
	n	$1s2p^2\ ^2S_{1/2} - 1s^22p\ ^2P_{1/2}$
	m	$1s2p^2\ ^2S_{1/2} - 1s^22p\ ^2P_{3/2}$
	s	$1s(2s2p^3P)^2P_{3/2} - 1s^22s\ ^2S_{1/2}$
	t	$1s(2s2p^3P)^2P_{1/2} - 1s^22s\ ^2S_{1/2}$

REFERENCES

1. B. Edlen, Symposium on Production and Physics of Highly Charged Ions, to appear in Physica Scripta, 1982.
2. K.W. Hill et al., AIP Proc. No. 75, 8 (1981) and PPPL-1887, April 1982.
3. N.J. Peacock, AIP Proc. No. 75, 101 (1981).
4. C. deMichelis and M. Mattioli, Nuclear Fusion 21, 677 (1981).
5. Equipe TFR, Nuclear Fusion 18, 647 (1978).
6. S. Suckewer, Physica Scripta 23, 72 (1981).
7. T. Kato et al, Institute of Plasma Physics, Nagoya, IPPJ-544, (1981).
8. E.S. Marmar et al., MIT/PFC Report JA-82-12 submitted for publication (1982).
9. R. Petrasso et al., Nuclear Fusion 21, 881 (1981), and Rev.Sci.Instr. 51, 585 (1980).
10. S. van Goeler, W. Stodiak, and N. Sauthoff, Phys.Rev.Lett 33, 1201 (1974), and N.R. Sauthoff, SPIE, Vol. 106, 40 (1977).
11. M. Bitter et al., in πInner Shell and X-ray Physics of Atoms and Solids (Plenum Press) 1981, p.861 and PPPL-78 6492.
12. J.E. Rice, K. Molvig, and H.I. Helava, Phys.Rev. A25, 1645 (1981).
13. S. van Goeler et al, Bull.Am.Phys.Soc. 26, 812 (1981).
14. K.W. Hill et al., Phys.Rev. A19, 1770 (1979), M.Bitter et al., Phys.Rev.Letter 43, 129 (1979), and M. Bitter et al., PPPL-1891, April 1982.
15. E. Kallne and J. Kallne, submitted to Physica Scripta (1982).
16. P. Platz et al., J.Phys.E 14, 448 (1981) and J.Phys. B15, 1007 (1981).
17. M.G. Hobby, N.J. Peacock, and J.E. Bateman, Culham Laboratory, CLM-R103 (1980).
18. G.L. Jahns et al., Nuclear Fusion 18, 609 (1978) and M.A. Dubois, D.A. Marty and A. Pochelon, Nucl.Fusion 20, 1355 (1980).
19. H. Knoepfel and D.A. Spong, Nucl.Fusion 9, 785 (1979).
20. E. Meservey et al., Bull.Am.Phys.Soc. 26, 981 (1981).
21. B. Blackwell et al., in Plasma Physics and Controlled Nuclear Fusion Research Proc. 9th Int.Conf., Baltimore 1982.
22. U.I. Safronova, Physica Scripta 23, 241 (1981).
23. L.A. Vainshtein and U.I. Safronova, Atomic Data Nuclear Data Tables 21, 49 (1978).
24. A.H. Gabriel, Mon.Not.R.Astr.Soc. 160, 99 (1972).
25. V.A. Boiko, et al., Mon.Not.R.Astr.Soc. 185, 789 (1978).
26. R.D. Cowan, Symposium on Production and Physics of Highly Charged Ions, Physica Scripta (1982), and E. Kallne, J. Kallne, and R.D. Cowan, submitted for publication (1982).
27. V.A. Boiko et al., J.Quant.Spectr.Rad.Transf. 19, 11 (1978).
28. J. Dubau and S. Volonte, Rep.Prog.Phys. 43,199 (1980).
29. U.I. Safronova, A.M.Urnov, and L.A. Vainshtein, Dielectronic Satellites for High Charged Resonance Lines, Preprint.
30. C.P. Bhalla, A.H. Gabriel, and L.P. Presnyakov, Mon.Not.R.Astr.Soc. 172, 359 (1975).
31. D.S. Pappas et al., Bull.Am.Phys.Soc. 26, 885 (1981) and J.E. Rice, private communication.
32. A.K. Pradhan, Astroph.J.(in press), and Phys.Rev. A23, 619 (1981).
33. E. Kallne, J. Kallne, and A.K. Pradhan, submitted for publication (1982).
34. E. Kallne, J. Kallne, and J.E. Rice, Phys.Rev.Lett. 49, 330 (1982).
35. V.L. Jacobs et al., Astroph.J. 230, 627 (1979).
36. J. Kallne, E. Kallne, L. Atencio, C. Morris, and A. Thompson, Nucl.Instr.Methods, Fall 1982 (to appear) and ibid Forth APS Topical Conf. on High Temp. Plasma Diagnostics, Boston, Aug. 25-27, 1982.
37. H.W. Schnopper and P.O. Taylor, U.S. Department of Energy Report No. E4-76-502-4021 (1977).
38. R.J. Hawryluk et al., Phys.Rev.Lett. 49, 326 (1982).

Figure Captions

Fig. 1: Radial emissivity profiles for He- and H-like S at T_e = 1400 eV assuming coronal equilibrium abundancies and measured radial distributions of N_e and T_e. The results are for the Alcator C tokamak at MIT with a plasma limiter of 16 cm radius.

Fig. 2: Temporal development of a typical Alcator C plasma hydrogen discharge at 60 kG magnetic field. The traces from top to bottom are plasma current (I_p = 325 kA at peak), electron density ($\bar{N}_e$ = 0.58 x $10^{14}cm^{-3}$/fringe), and the count rates of soft X-ray diode (E >1 keV) and high resolution X-ray spectrometer (at Cl^{15+} 4.44 Å).

Fig. 3: Schematics of cylindrical crystal geometry showing slit, crystal and detector to scale. The crystal used is PET 2d = 8.742 Å, $\mathcal{S}$ = 59.5 cm at a Bragg angle of 33.5°.

Fig. 4: Full bandwidth spectrum composed of three different detector settings each being a sum of four similar plasma discharges at $\bar{N}_e$ = 2.3 x $10^{14}cm^{-3}$ and T_e ~1.4 keV. The Mo emission is enhanced relative to that of S and Cl for these conditions.

Fig. 5: H-like spectrum of sulphur showing the 1s-2p resonance doublet as well as the dielectronic recombination satellite line J. Some $n \geq 3$ satellites can also be discerned. The solid lines are fits to the peaks. The spectrum is a sum of eight similar discharges of deuterium with $\bar{N}_e$ = 3.5 x $10^{14}cm^{-3}$, T_e ~ 1.25 keV and B_T = 80 kG.

Fig. 6: He-like spectrum of Cl showing the principal lines w, x, y, and z as well as the satellites q, r, a and k. The spectrum is a sum of twenty discharges in deuterium with $\bar{N}_e \approx 1.5 \times 10^{14}cm^{-3}$, $T_e \approx$ 760 eV and B_T = 40 kG. Also observed are satellites to the He-like 1s-3p resonance in Sulphur the strongest of which lies at 4.388 A.

Fig. 7: Same as in Figure 6 but for a sum of twelve discharges in hydrogen of the conditions $\bar{N}_e$ = 2.9 x $10^{14}cm^{-3}$, T_e = 940 eV and B_T = 80 kG.

Fig. 8: The experimental spectrum of Figure 6 with three-point smoothing. The strongest lines of the predicted[29] satellite spectrum of He-like Cl are shown with intensities normalized to the measured k line. All intensities are from dielectronic recombination except for lines q and r where the added effect of inner shell excitation is shown by the broken line.

Fig. 9: Example of He-like spectra for sulphur recorded for a <u>single</u> plasma discharge. The conditions were $\bar{N}_e$ = 3 x $10^{14}cm^{-3}$, $T_e \approx$ 1.8 keV and B_T = 80 kG for a plasma of deuterium.

Fig. 10: Example of detector setting selected to record the H-like and He-like simultaneously. Besides the 1s-2p resonance lines, one can see the satellite line J and the 2p-3d line of Mo^{32+} at 4.804 A. Plasma discharge in hydrogen with conditions of $N_e = 3.5 \times 10^{14} cm^{-3}$, T_e 1.8 keV, and $B_T = 80$ kG.

Fig. 11: Example of He-like spectrum of chlorine from single plasma discharge - deuterium with conditions of $\overline{N}_e = 3.5 \times 10^{14} cm^{-3}$ and $B_T = 80$ kG.

Fig. 12: Example of spectrum in the region of the H-like resonance line in sulphur with intensity variation in line Mo-emission. Plasma discharges in deuterium with $\overline{N}_e = 2.3 \times 10^{14} cm^{-3}$ and $B_T = 80$ kG. The temperature is determined to be $T_e = 1.6$ and 1.8 keV for (a) and (b) as discussed in the text.

Fig. 13: Example of intensity variation in the ratio x/y for He-like Cl between nominally similar (single) plasma discharge in deuterium with conditions of $\overline{N}_e = 3.4 \times 10^{14} cm^{-3}$, $T_e \approx 1.4$ keV, and $B_T = 80$ kG.

Fig. 14: Example of intensity variations in the ratio $W(P_{1/2})/W(P_{1/2})$ for H-like sulphur for two consecutive, similar plasma discharges in deuterium of the conditions of $\overline{N}_e \approx 2.5 \times 10^{14} cm^{-3}$, $T_e \approx 1.4$ keV and $B_T = 80$ kG.

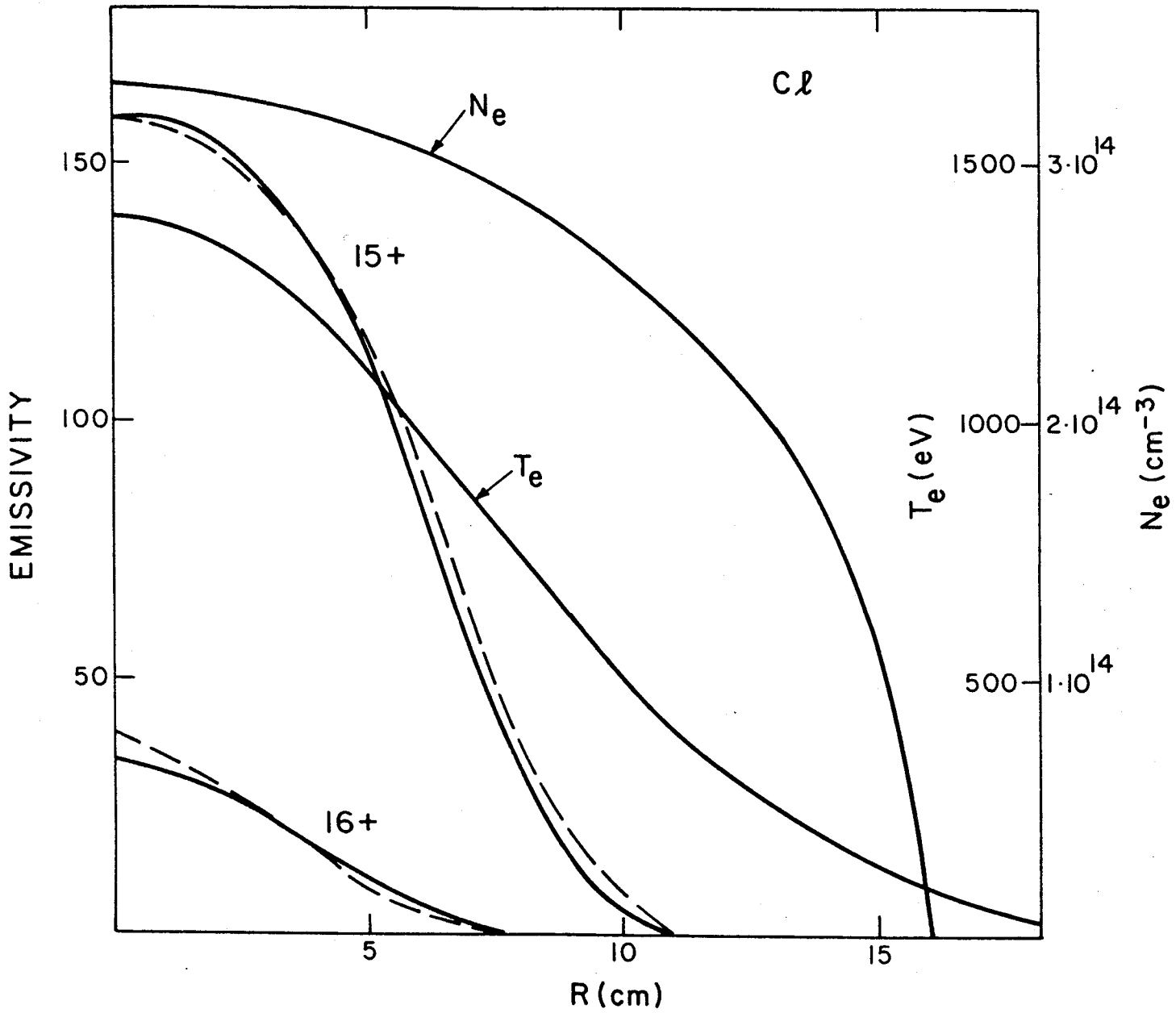
Cℓ
N_e
15+
T_e
16+
EMISSIVITY
150
100
50
1500
1000
500
$3\cdot10^{14}$
$2\cdot10^{14}$
$1\cdot10^{14}$
T_e (eV)
N_e (cm^{-3})
5
10
15
R (cm)

Figure 1

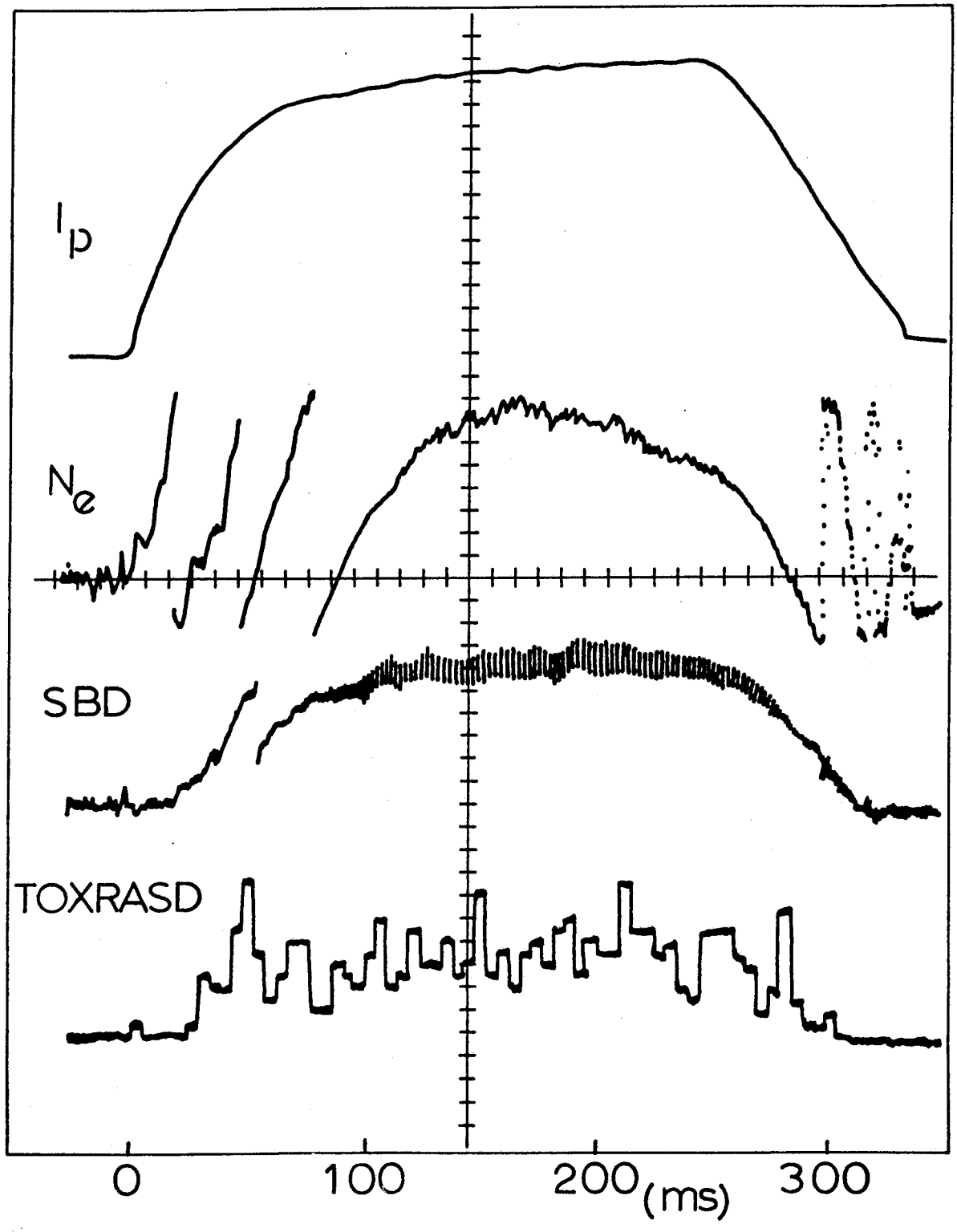

Figure 2

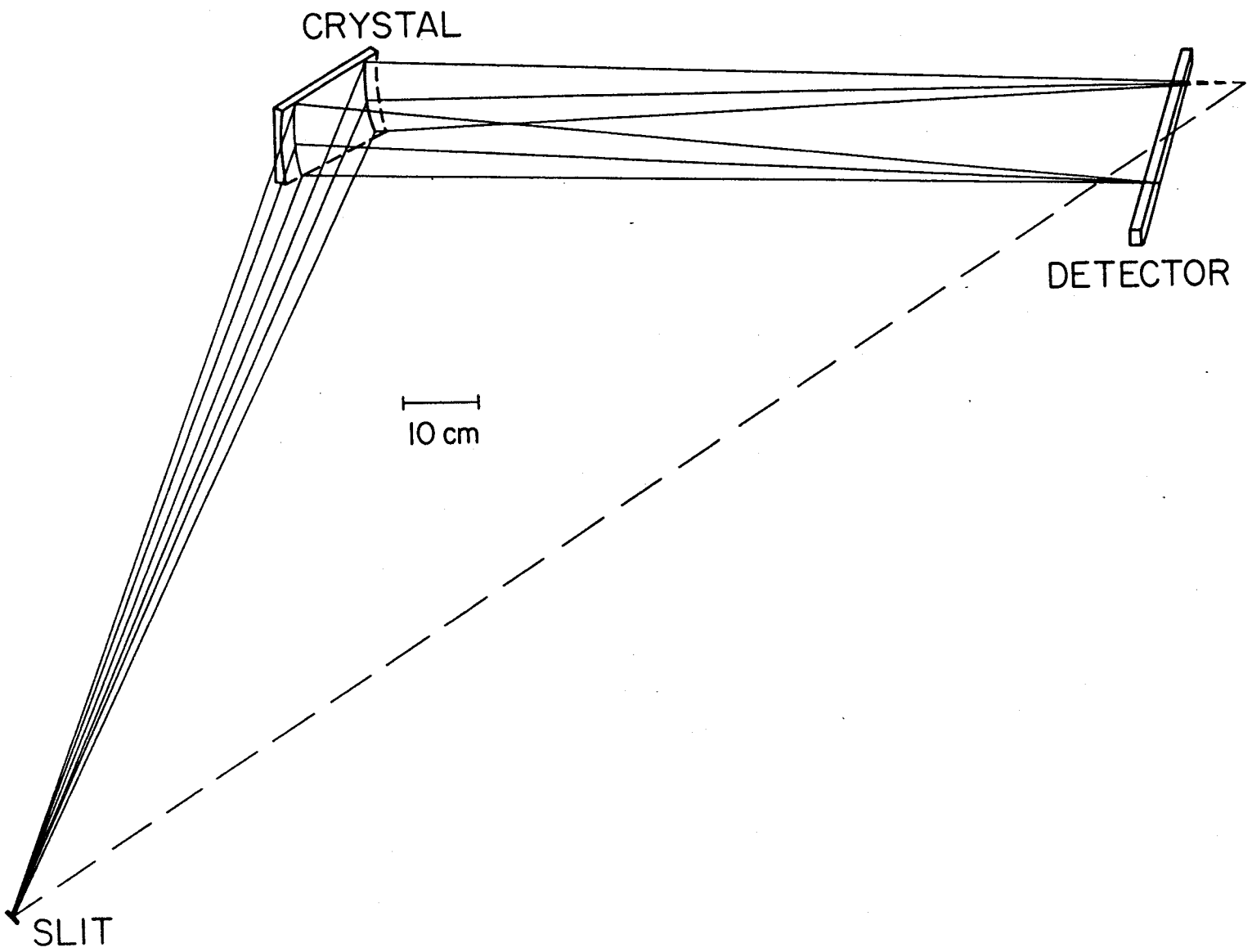

Figure 3

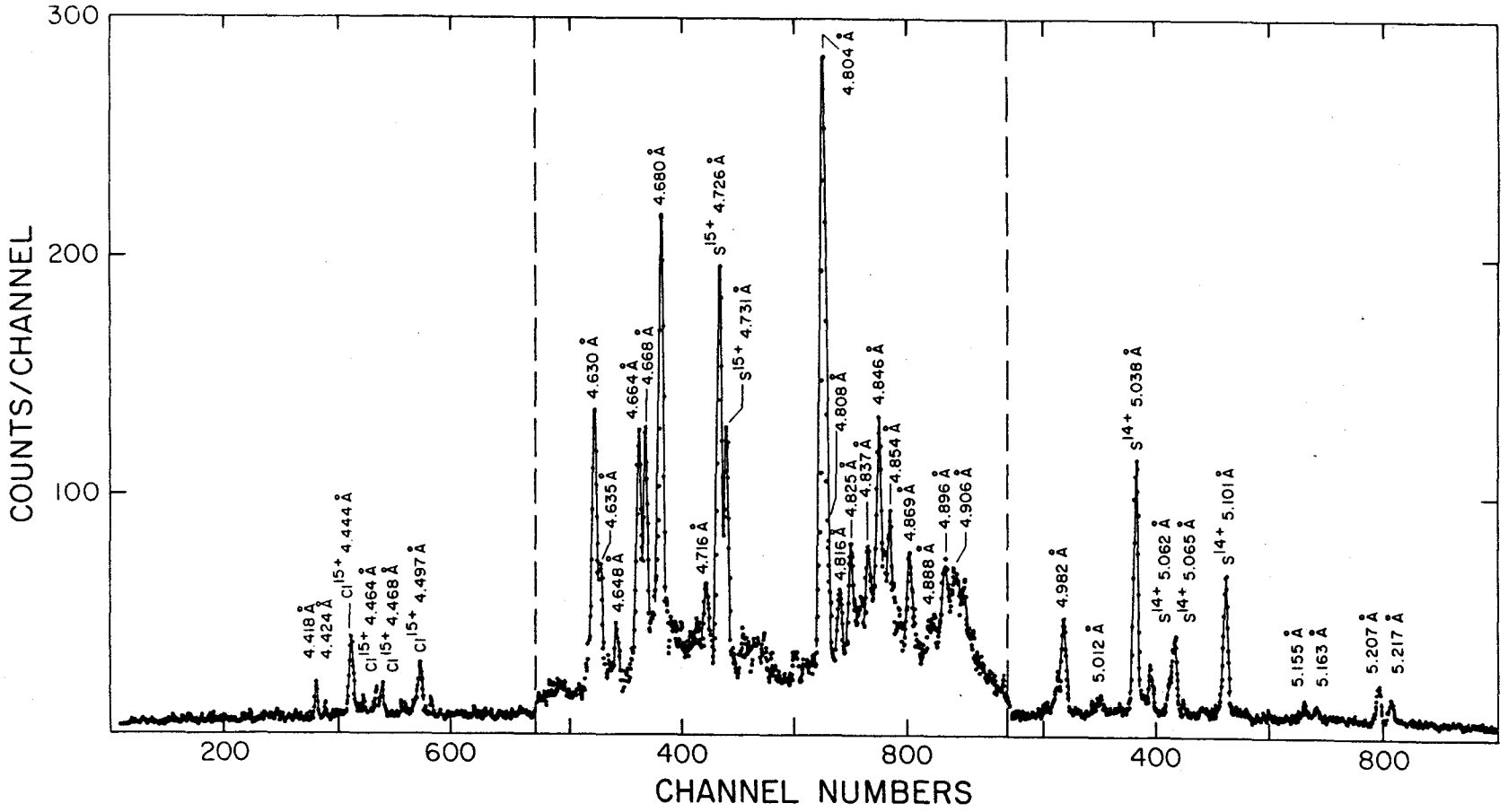
COUNTS/CHANNEL
300
200
100
200
600
400
800
400
800
CHANNEL NUMBERS
4.418 Å
4.424 Å
Cl15+ 4.444 Å
Cl15+ 4.464 Å
Cl15+ 4.468 Å
Cl15+ 4.497 Å
4.630 Å
4.635 Å
4.648 Å
4.664 Å
4.668 Å
4.680 Å
4.716 Å
S15+ 4.726 Å
S15+ 4.731 Å
4.804 Å
4.808 Å
4.816 Å
4.825 Å
4.837 Å
4.846 Å
4.854 Å
4.869 Å
4.888 Å
4.896 Å
4.906 Å
4.982 Å
5.012 Å
S14+ 5.038 Å
S14+ 5.062 Å
S14+ 5.065 Å
S14+ 5.101 Å
5.155 Å
5.163 Å
5.207 Å
5.217 Å

Figure 4

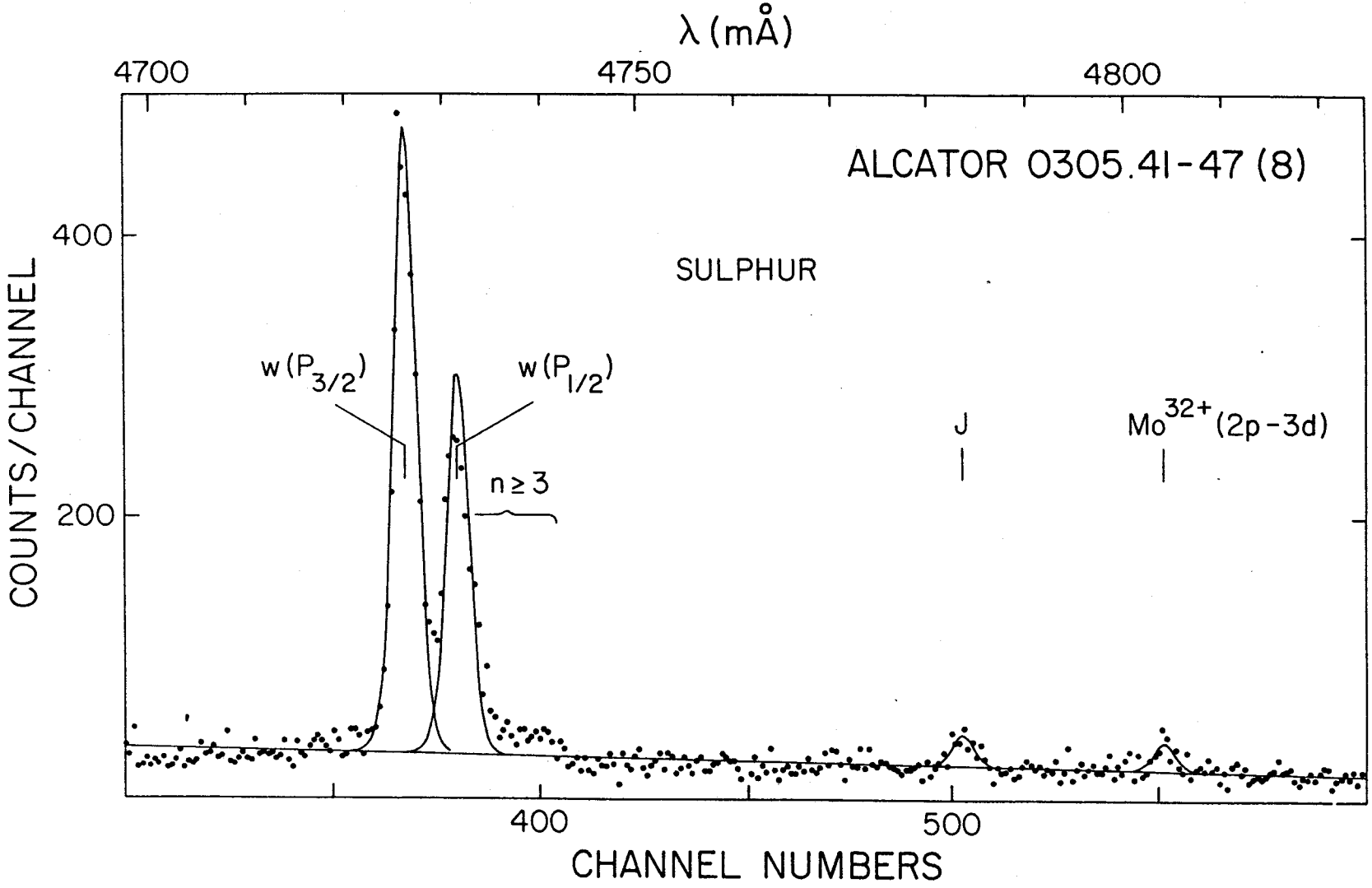
λ (mÅ)
4700
4750
4800
ALCATOR 0305.41-47 (8)
SULPHUR
400
200
COUNTS/CHANNEL
w(P3/2)
w(P1/2)
n≥3
J
Mo32+ (2p-3d)
400
500
CHANNEL NUMBERS

Figure 5

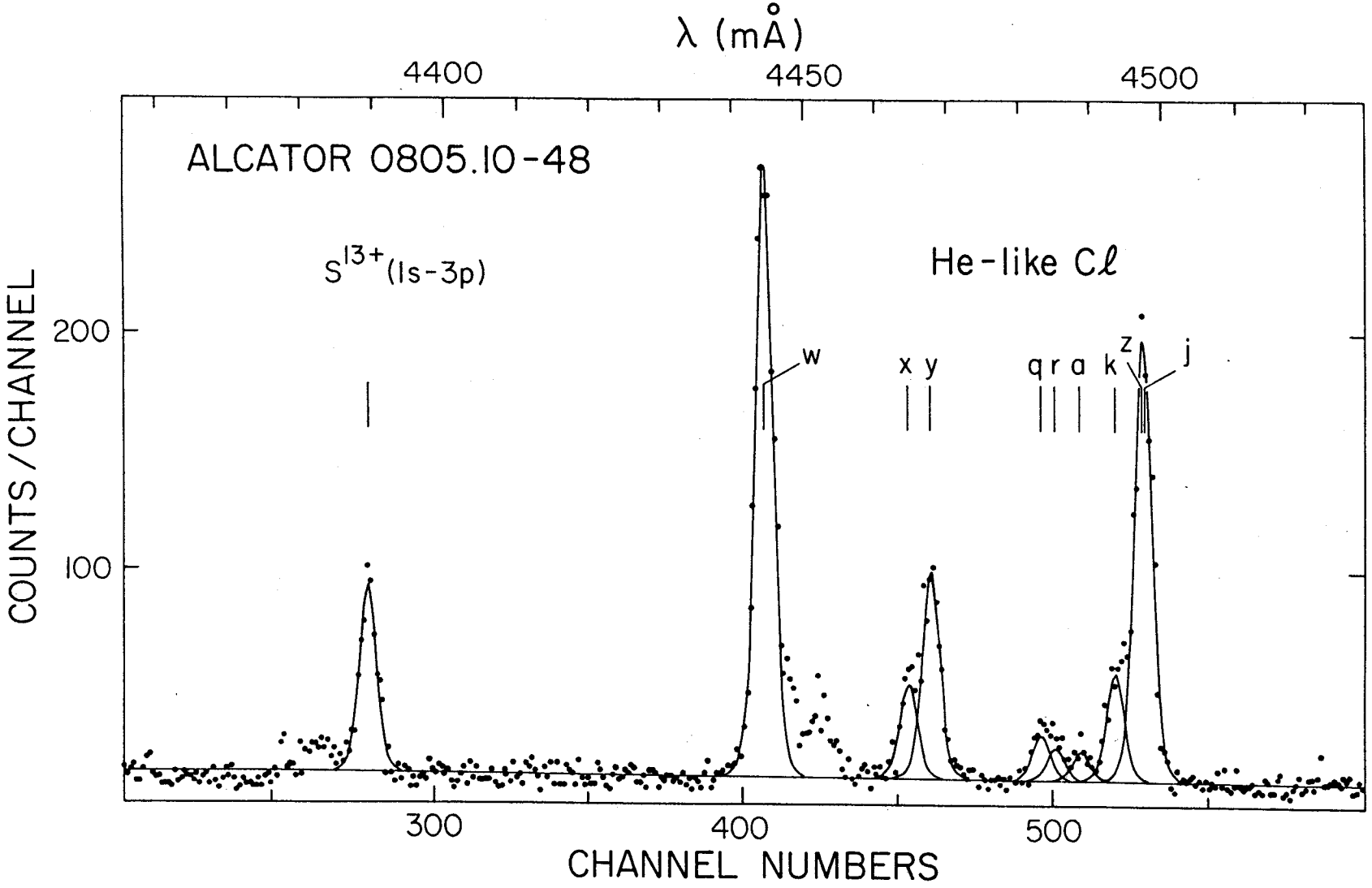
λ (mÅ)
4400
4450
4500
ALCATOR 0805.10-48
S13+(1s-3p)
He-like Cℓ
w
x y
q r a k
z
j
COUNTS/CHANNEL
200
100
300
400
500
CHANNEL NUMBERS

Figure 6

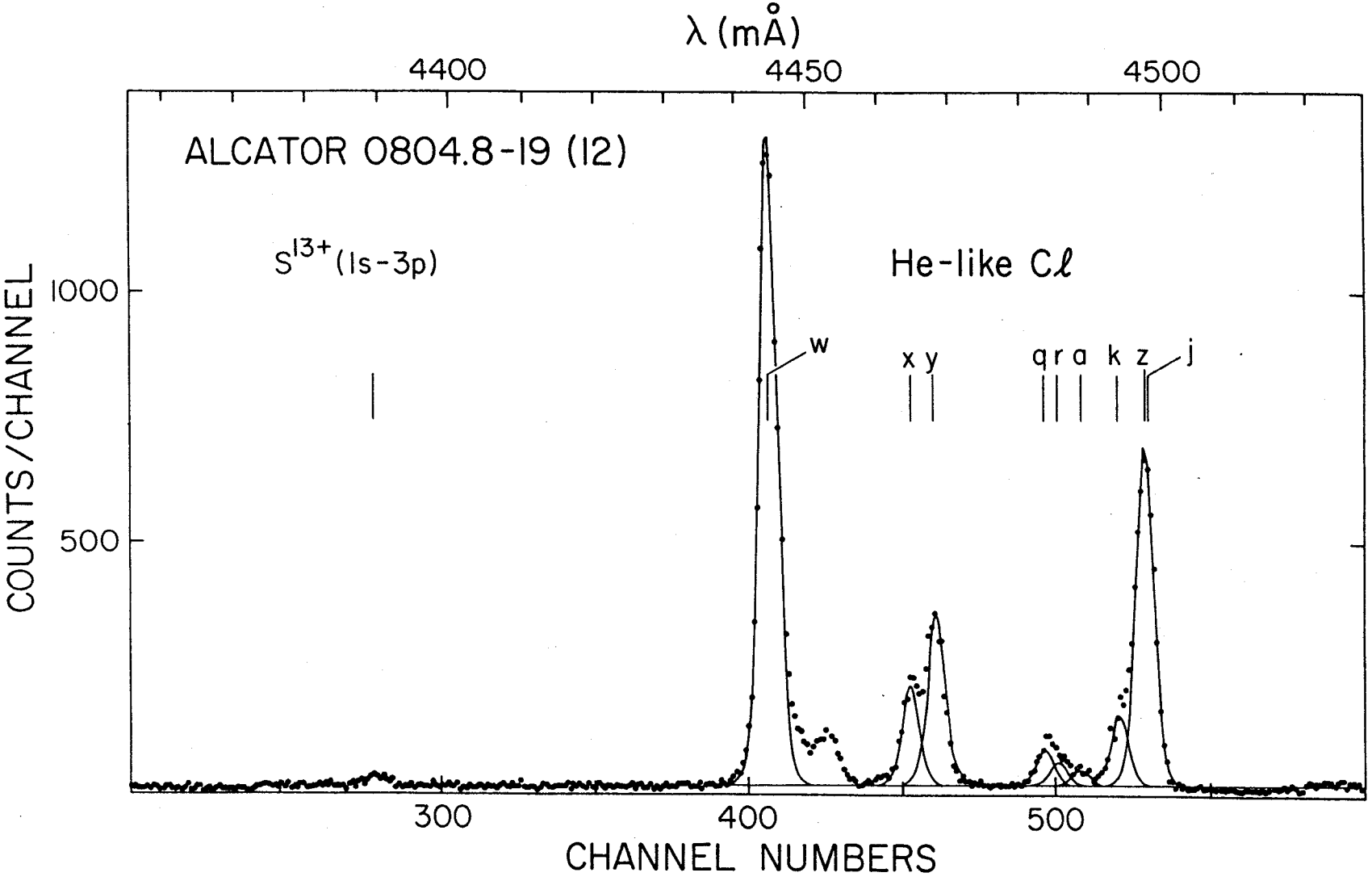
λ (mÅ)
4400
4450
4500
ALCATOR 0804.8-19 (12)
S^{13+} (1s-3p)
He-like Cℓ
w
x y
q r a k z j
COUNTS/CHANNEL
1000
500
300
400
500
CHANNEL NUMBERS

Figure 7

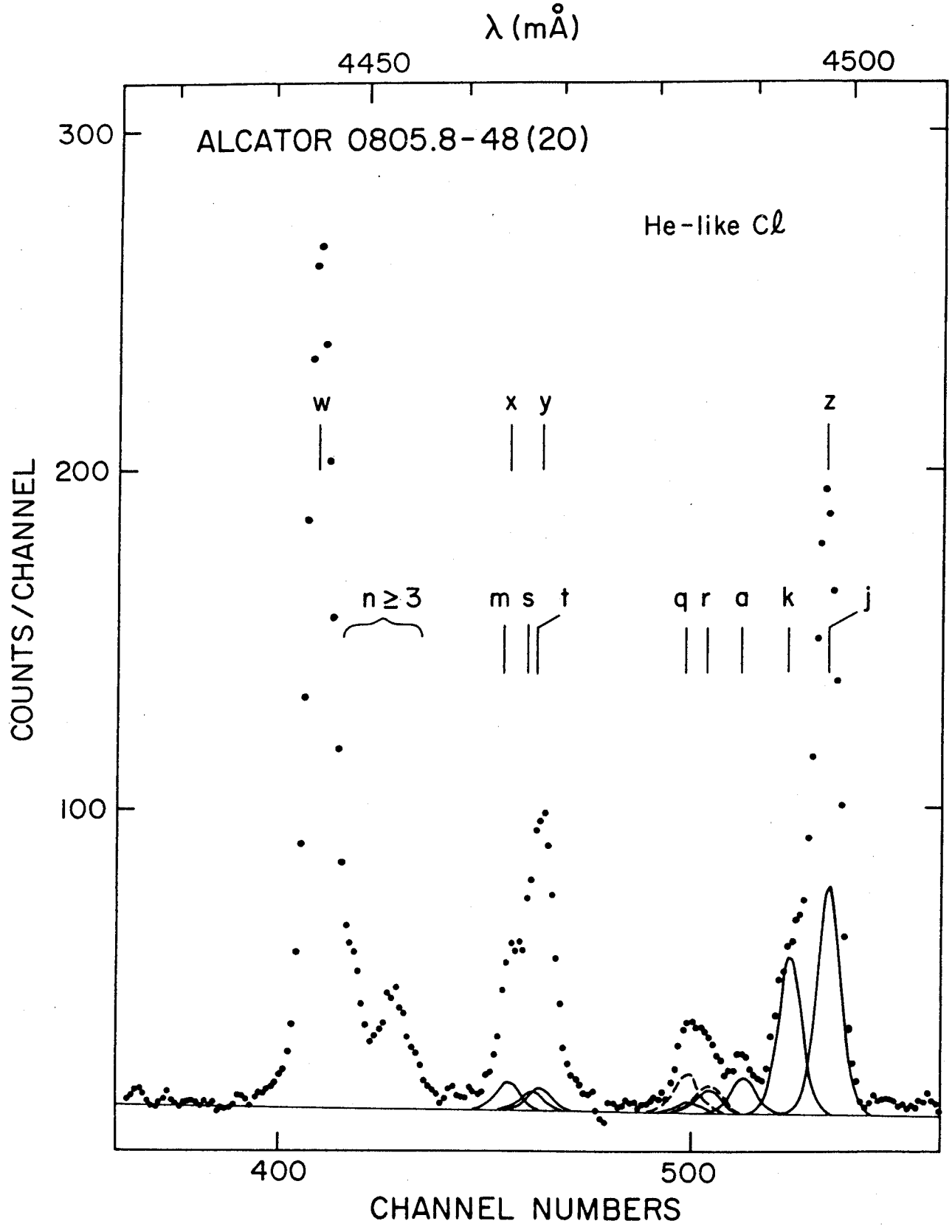
λ (mÅ)
4450
4500
ALCATOR 0805.8-48(20)
He-like Cl
300
200
100
COUNTS/CHANNEL
w
x y
z
n≥3
m s t
q r a k
j
400
500
CHANNEL NUMBERS

Figure 8

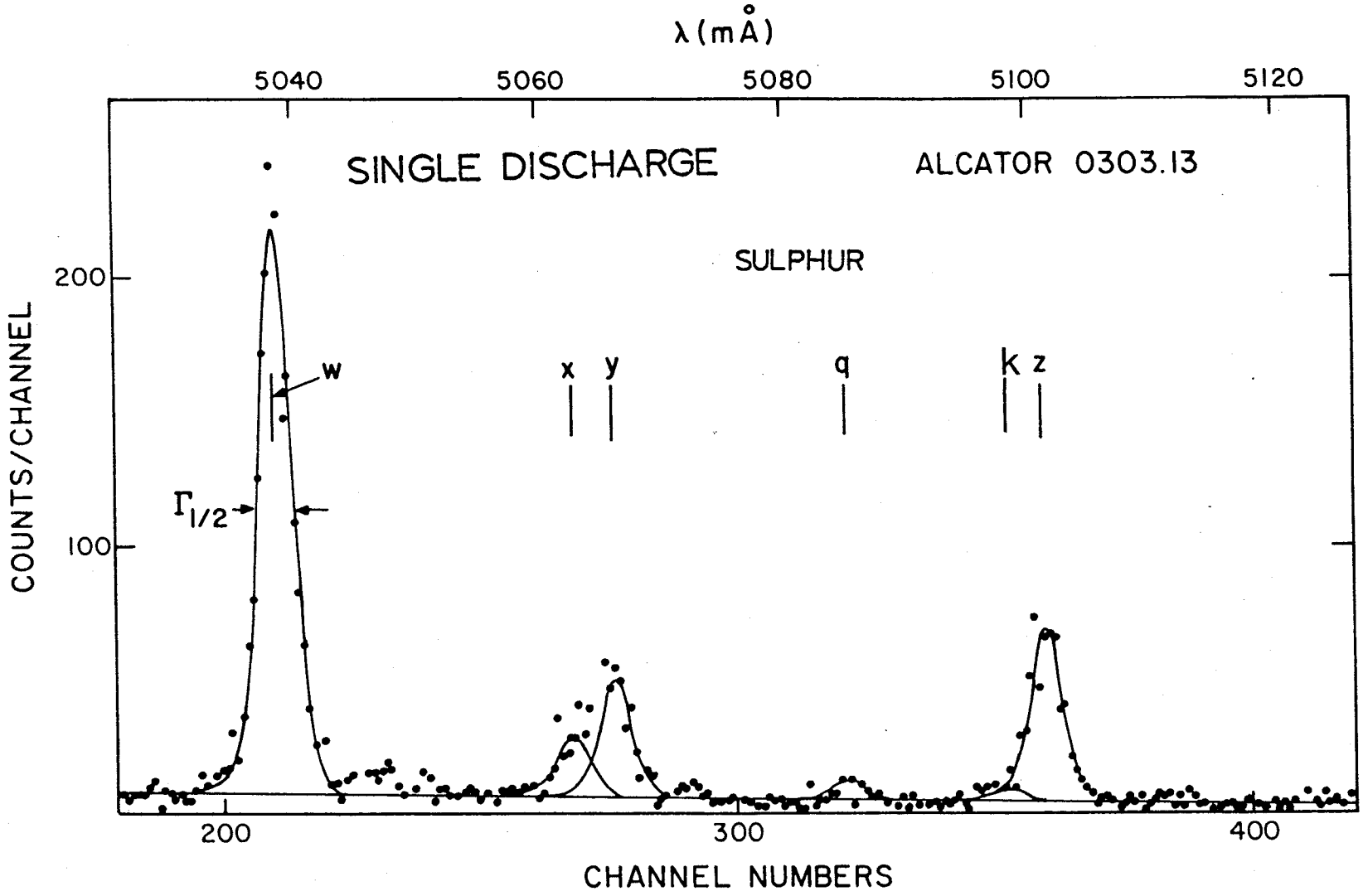
λ (mÅ)
5040
5060
5080
5100
5120
SINGLE DISCHARGE
ALCATOR 0303.13
SULPHUR
200
100
COUNTS/CHANNEL
w
x
y
q
k
z
$\Gamma_{1/2}$
200
300
400
CHANNEL NUMBERS

Figure 9

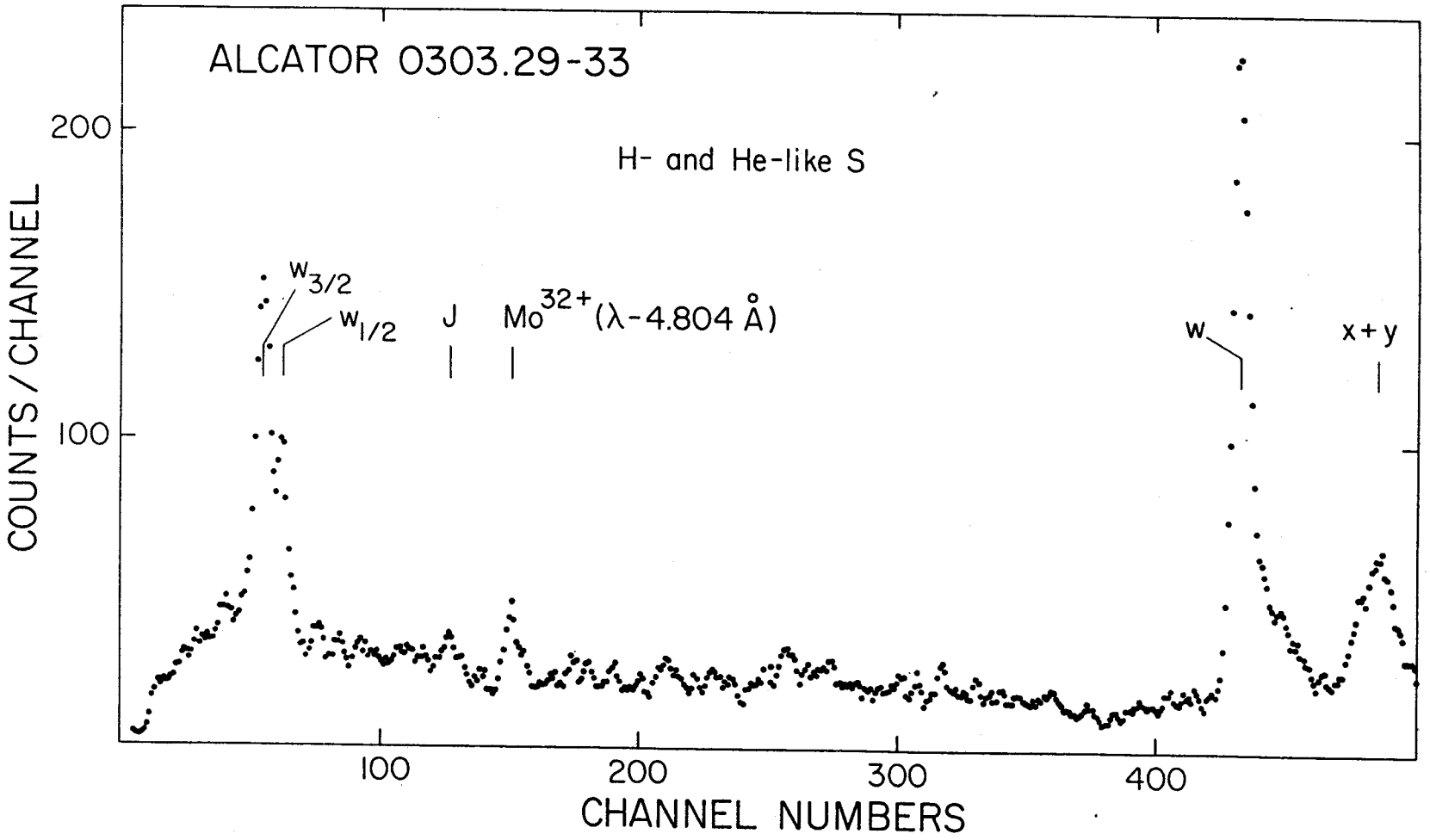
ALCATOR 0303.29-33
H- and He-like S
$W_{3/2}$
$W_{1/2}$
J
Mo^{32+} (λ-4.804 Å)
W
x+y
COUNTS / CHANNEL
200
100
100
200
300
400
CHANNEL NUMBERS

Figure 10

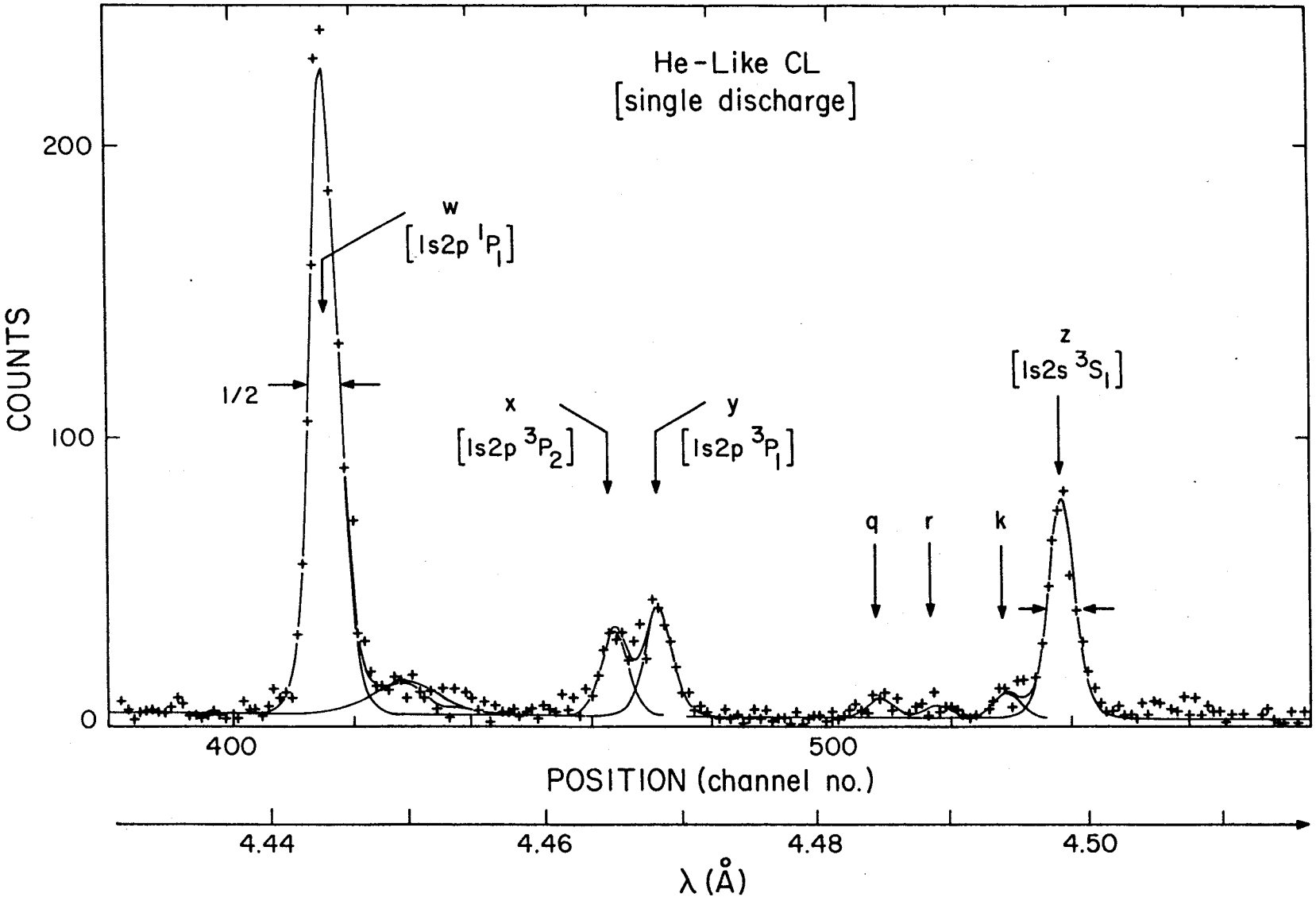
He-Like CL
[single discharge]
COUNTS
200
100
0
w
[1s2p $^1P_1$]
1/2
x
[1s2p $^3P_2$]
y
[1s2p $^3P_1$]
z
[1s2s $^3S_1$]
q
r
k
400
500
POSITION (channel no.)
4.44
4.46
4.48
4.50
λ (Å)

Figure 11

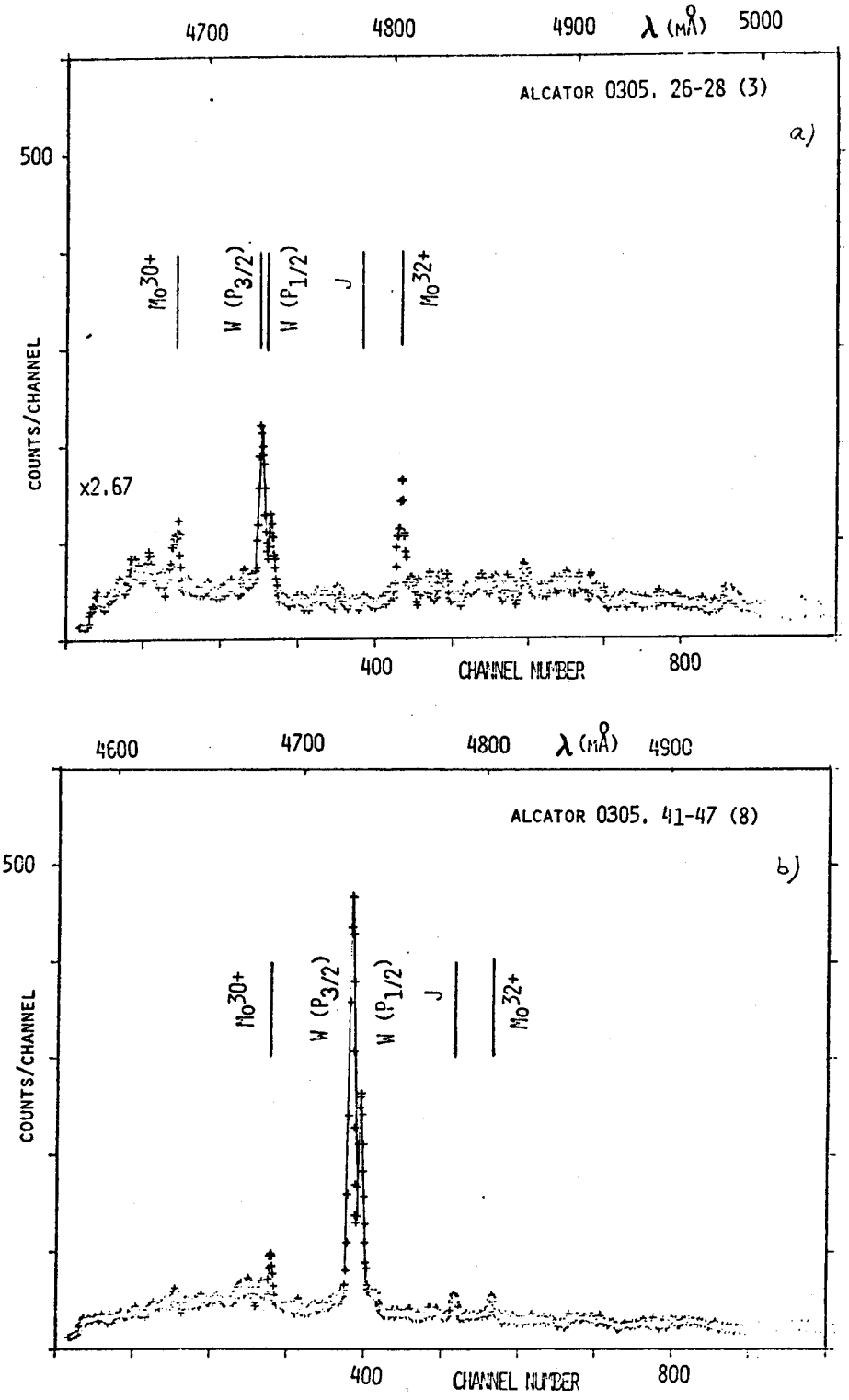
4700
4800
4900
λ (mÅ)
5000
ALCATOR 0305, 26-28 (3)
a)
500
Mo^{30+}
W ($P_{3/2}$)
W ($P_{1/2}$)
J
Mo^{32+}
COUNTS/CHANNEL
x2.67
400
CHANNEL NUMBER
800
4600
4700
4800
λ (mÅ)
4900
ALCATOR 0305, 41-47 (8)
b)
500
Mo^{30+}
W ($P_{3/2}$)
W ($P_{1/2}$)
J
Mo^{32+}
COUNTS/CHANNEL
400
CHANNEL NUMBER
800

Figure 12

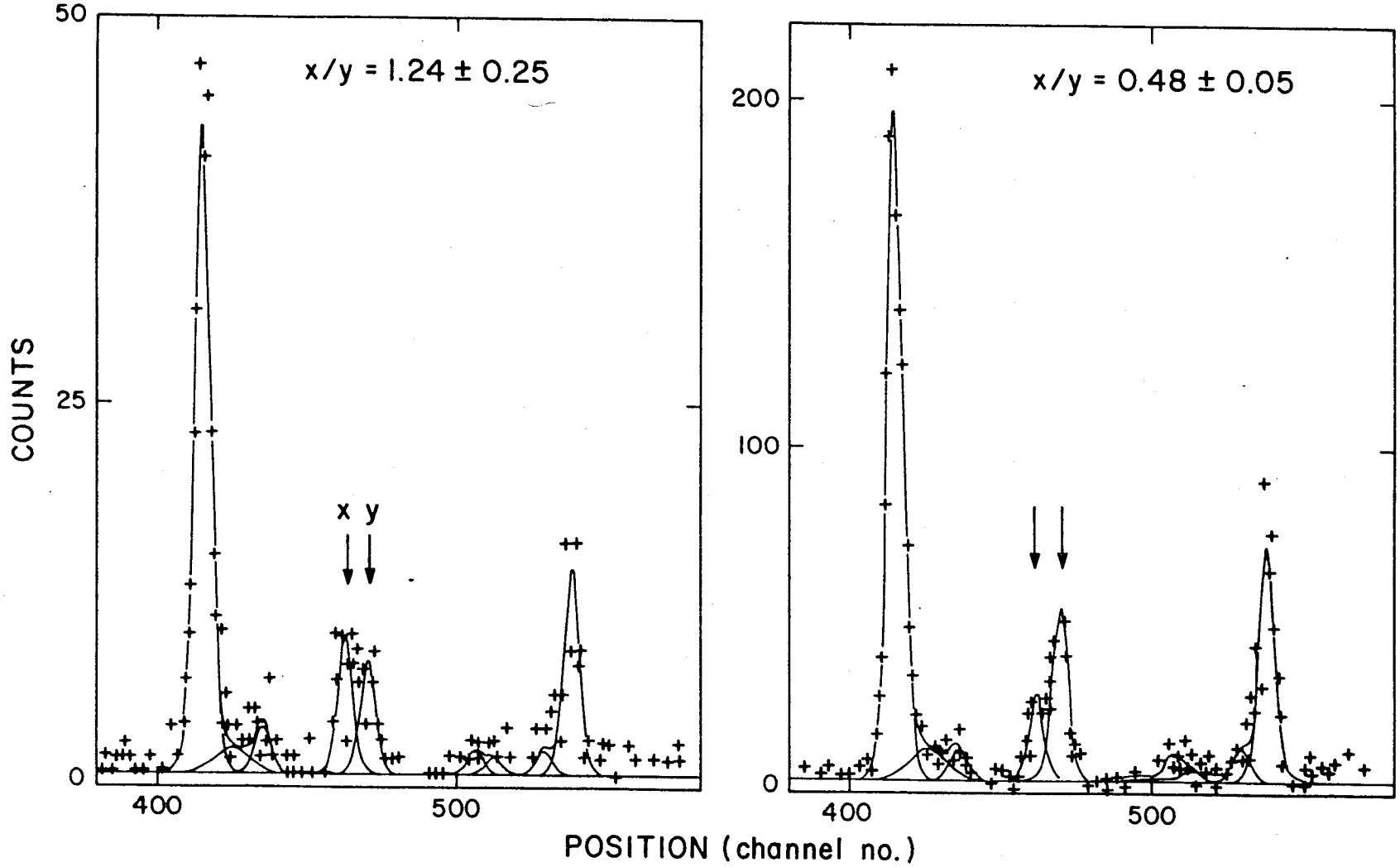
x/y = 1.24 ± 0.25
x/y = 0.48 ± 0.05
x y
COUNTS
POSITION (channel no.)
50
25
0
200
100
400
500

Figure 13

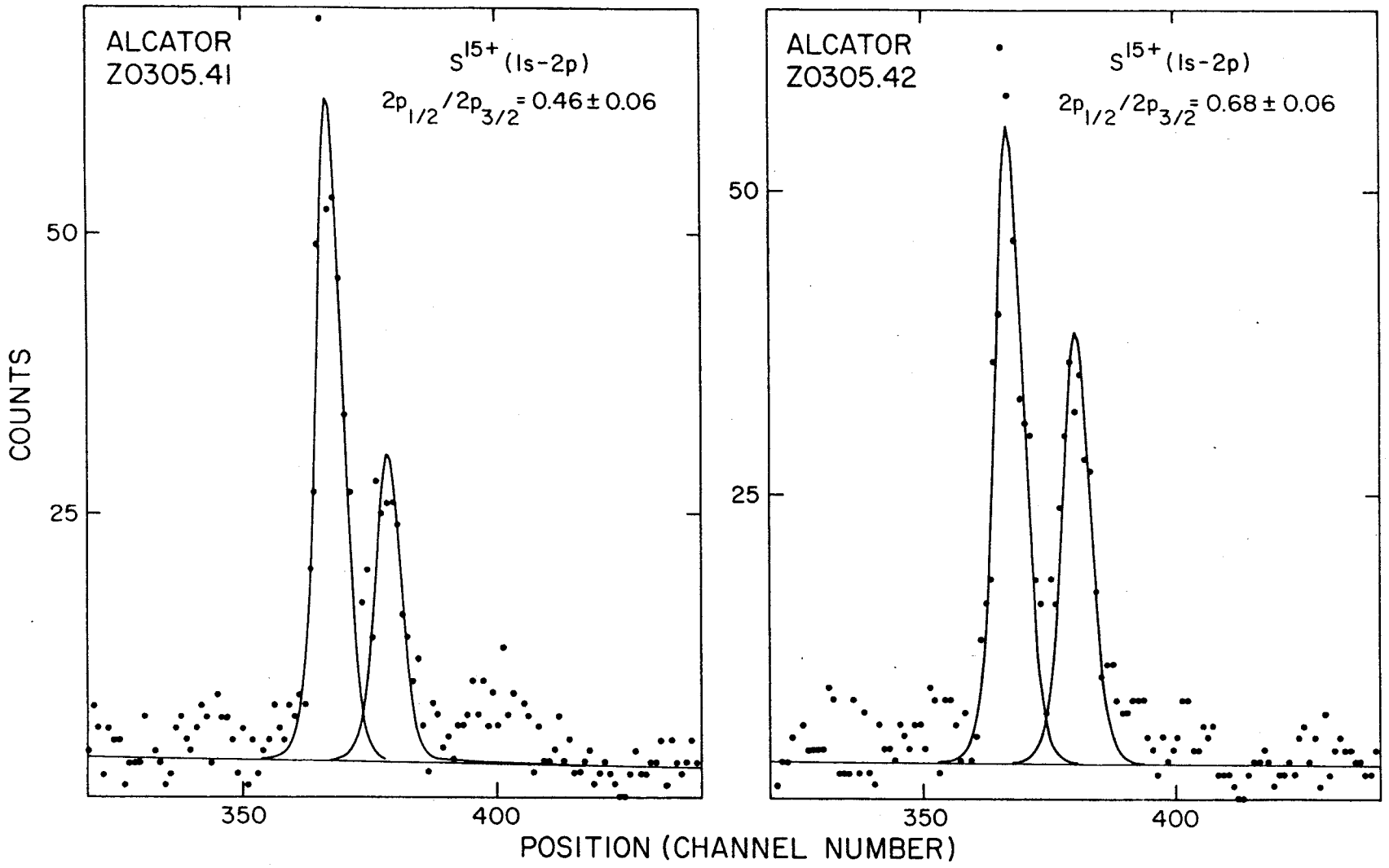
ALCATOR
Z0305.41
S^{15+} (1s-2p)
$2p_{1/2}/2p_{3/2} = 0.46 \pm 0.06$
ALCATOR
Z0305.42
S^{15+} (1s-2p)
$2p_{1/2}/2p_{3/2} = 0.68 \pm 0.06$
COUNTS
50
25
350
400
POSITION (CHANNEL NUMBER)

Figure 14